# Tensile study of melt-spun poly(3-hydroxybutyrate) P3HB fibers: Reversible transformation of a highly oriented phase

*Edith Perret*[a,b,⊥], *Felix A. Reifler*[a, b,⊥], *Ali Gooneie*[a], *Rudolf Hufenus*[a, *]

[a] Laboratory for Advanced Fibers, Empa, Swiss Federal Laboratories for Materials Science and Technology, Lerchenfeldstrasse 5, 9014 St. Gallen, Switzerland

[b] Center for X-ray Analytics, Empa, Swiss Federal Laboratories for Materials Science and Technology, Überlandstrasse 129, 8600 Dübendorf, Switzerland

for Table of Contents use only

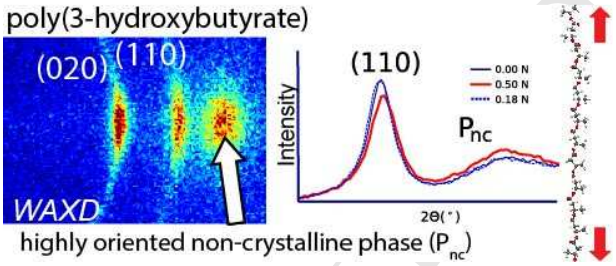


KEYWORDS: poly(3-hydroxybutyrate), P3HB, melt-spun fibers, melt spinning, biopolymer, WAXD, SAXS, x-ray diffraction

ABSTRACT

Poly-3-hydroxybutyrate (P3HB) typically crystallizes into the orthorhombic α-form. The additional intense and rather broad equatorial reflection in wide-angle X-ray diffraction (WAXD) patterns seen in our melt-spun P3HB fibers cannot be attributed to the α-form crystals. We propose that a non-crystalline mesophase, which consists of disordered but highly oriented and stretched molecules located between α-crystals, leads to the observed broad equatorial reflection. We show that the transformation of this mesophase from and into the α-form phase is partially reversible under cyclic tensile loading. Structure factor calculations, which are based on atomic positions from molecular dynamics simulations of a set of stretched P3HB molecules, support this model. The WAXD patterns were analyzed with azimuthal, radial, equatorial and meridional scans and the changes in the crystal orientation, changes in the percentages of individual phases and changes in the α-crystal lattice spacings were analyzed as a function of the applied tension. Changes in long spacings, crystal sizes and coherence lengths under cyclic loading were determined with small-angle X-ray scattering (SAXS) measurements. The long spacing between α-crystals increases when tensile stress is applied and it snaps back to the original spacing when the tensile stress is released.

## INTRODUCTION

Polyhydroxybutyrate (PHB) is a type of a polyhydroxyalkanoate (PHA) biopolyester, synthesized by microorganisms as intracellular organic inclusions serving as energy storage [1]. Farming these microorganisms (bacteria) and feeding them sugar, starch or other carbon sources enables the microbial mass production of PHB on an industrial scale [1-4]. Poly-3-hydroxybutyrate (P3HB) is the most common PHB and has been extensively studied in the past [5, 6].

Biopolymers stored in vivo remain in the amorphous state, while in the isolated state, the polymer rapidly crystallizes [1]. Typically P3HB has poor impact strength, because of the slow secondary crystallization that occurs after processing. The low nucleation density can result in large spherulites (spherulitic aggregates of lamellar crystals) [1, 2]. However, this secondary crystallization can be prevented by establishing a lamellar morphology during processing. Therefore, drawn P3HB films and fibers do not undergo secondary crystallization, and the mechanical properties of drawn and annealed P3HB remain unchanged, at least for several months [7-9].

Our group obtained filaments dominated by longitudinally oriented lamellae by installing the take-up godet at an unusually short distance from the spinneret. In this way, secondary crystallization was hindered, and the melt-spun filaments show long-term stability and comply with requirements for textile manufacturing [8].

P3HB typically crystallizes in the orthorhombic α-form, which is characterized by a left-handed $2_1$ helix conformation of the P3HB chains [10, 11]. Yokouchi et al. [12] were the first authors who have observed an additional intense equatorial reflection and streaks above the layer lines in a WAXD pattern of a highly stretched P3HB film, which cannot be assigned to the α-

form P3HB crystal structure. In the literature, these stress-induced additional reflections have been attributed to arise from a (para)crystalline β-form, which has been described to develop in the regions between α-form lamellar crystals by orientation of molecular chains [7, 9, 10, 12-16]. It has been suggested that the helical structure of the P3HB macromolecules from the α-form transforms into a planar zigzag conformation in oriented crystalline fiber systems [14]. Simulations of this deformation process have been done by Tanaka et al. [16]. Very recently, Phongtamrug and Tashiro et al. [17] are the first authors to suggest a crystal structure for the β-form, where chains are packed in a hexagonal unit cell with $a=b=9.22$ Å, $c=4.66$ Å and with a space group of $P3_221$.

In the present study, we have performed a thorough in-situ WAXD and SAXS study on melt-spun P3HB fibers under tensile loading. The materials used for the melt spinning of P3HB fibers and information about the experimental setups of the in-situ WAXD/SAXS measurements are given in the experimental section. The detailed analysis of WAXD/SAXS patterns given in the results/discussion section supports our hypothesis that the origin of the additional equatorial reflection in WAXD patterns from our melt-spun fibers is a highly oriented *non-crystalline mesophase* ($P_{nc}$), which is locally trapped between the aligned lamellae of the crystalline α-phase. The non-crystallinity of such a mesophase is also supported by molecular dynamics simulations and structure factor calculations.

## EXPERIMENTAL SECTION

### *Materials*

Two fiber samples were melt-spun from modified P3HB provided by Biomer (Krailling, Germany) on a customized pilot melt spinning plant originally built by Fourné Polymertechnik

(Alfter-Impekoven, Germany). In order to prevent crystallization of the extrudate in a randomly oriented state, the draw-off unit had to be modified by introducing a take-up godet which was mounted at an unusually short distance (0.75 m) from the spinneret. With this modified draw-off unit, fiber sample no. 974 was melt-spun with a draw ratio of seven from ready-to-use modified P3HB pellets ($M_w$ = 0.5 MDa), whereas raw P3HB powder ($M_w$ = 1.6 MDa), mixed with 20 wt% plasticizer (tri-n-butyl citrate (TBC)), was used to melt-spin fiber sample no. 1108 with a draw ratio of six. The P3HB pellets used for the former sample (no. 974) contained a nucleating agent (boron nitride (BN)) and 20 wt% TBC as well as various other processing aids, including low molecular weight poly-ε-caprolactone (PCL). The fiber diameters are about 90 µm for both fibers. More detailed information about materials, melt spinning parameters, and the properties of both P3HB fibers can be found in our previous publication [8]. For simplicity we label fiber no. 974 with (I) and fiber no. 1108 with (II) in the further course of this publication.

***In-situ WAXD and SAXS of fibers under tensile stress***

WAXD patterns of both fibers and SAXS patterns of fiber (I) were recorded on a Bruker Nanostar U diffractometer (Bruker AXS, Karlsruhe, Germany) with a beam defining pinhole of 300 µm, with Cu Kα radiation (λ = 1.5419 Å) and a VÅNTEC-2000 MikroGap area detector. The tensile stress was applied using a TS 600 tensile stage (Anton Paar GmbH, Graz, Austria) equipped with load cell LC-5N being capable of measuring forces up to 5 N. The calculation of applied tensile stresses is given in the data in brief article [18]. Single filaments were used for all WAXD and SAXS measurements, which were performed in two separate experiments with distances of 16.8 cm and 144.4 cm, respectively, between the sample and the active detector area. The filaments were glued on top of supports and held by tensile stage grips. The filaments

were elongated stepwise at an elongation rate of 0.1 mm/min. During elongation, the measured force increased, and the elongation step was automatically stopped when the pre-set nominal force value for the respective step was reached. Immediately after stopping, a WAXD pattern was recorded for 30 minutes or a SAXS pattern was recorded for two hours, respectively. During data collection, the grip position was kept constant by the tensile stage mechanism, while the filament underwent some relaxation. This relaxation resulted in a lower starting force for the subsequent step.

The recorded WAXD/SAXS patterns were analyzed with the evaluation software DIFFRAC.EVA (version 4.2., Bruker AXS, Karlsruhe, Germany) and python codes. Real space *d*-spacings between planes corresponding to $2\Theta_B$ values of the respective (hkl) reflections were calculated applying Bragg's law [19]. Peaks in, e.g., azimuthal WAXD scans were fit with Pearson VII distribution functions using python codes [20]. Herman's equation [18] was applied in order to extract the orientation parameter $f_{(hk0)}$ of the α-form crystals [21]. If $f_{(hk0)} = 1$ then the (hk0) planes of the crystals are completely aligned parallel to the fiber axis and if $f_{(hk0)} = 0$, then the crystals are randomly oriented. Long-spacings, coherence lengths and lamellar sizes were calculated by analyzing meridional and transversal areas of the SAXS pattern [18]. The performed intensity corrections to the WAXD/SAXS patterns due to the thinning of the fibers under tensile stress are explained in the data in brief article [18].

We have verified that the crystal structure of the P3HB fibers does not significantly change with time and have measured WAXD patterns two years after fiber production. No significant changes in the crystal structure have occurred at room temperature over a time period of several years.

RESULTS AND DISCUSSION

## 1. *Origin of additional equatorial reflection between 17.8 and 20.5°*

### *1.1. Arguments for a highly-oriented non-crystalline mesophase*

In-situ WAXD patterns from fiber (I) are shown in **Figure 1** for increasing tensile stress.

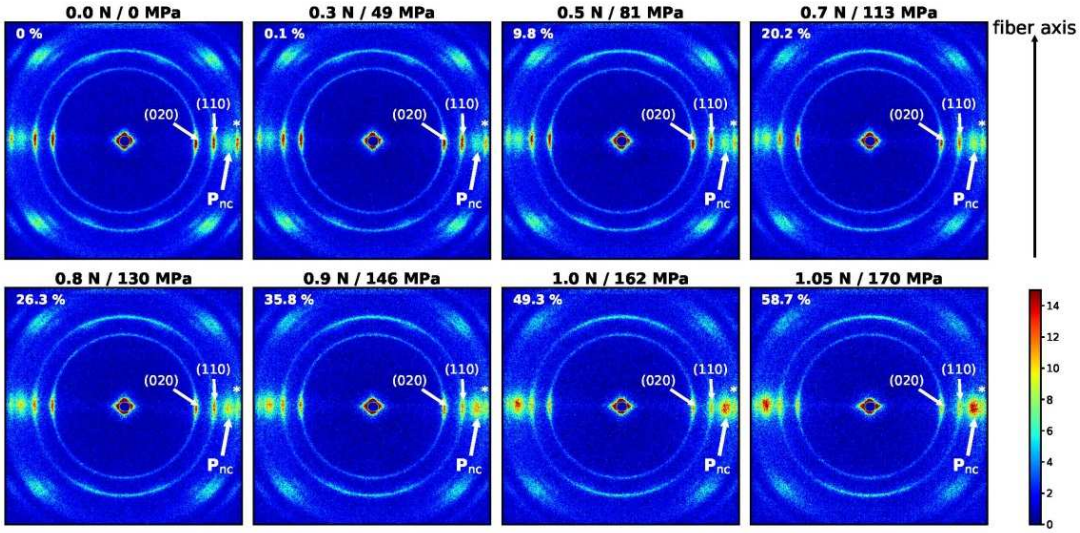


**Figure 1.** In-situ WAXD patterns of fiber (I) under increasing tensile stress. The applied force to the fiber and the resulting stress are indicated above each WAXD pattern and strains are indicated in the upper left corner. Breakage of the fiber occurred when applying a stress above 170 MPa.

The equatorial reflections (020) and (110) are indexed with respect to the orthorhombic unit cell (a=5.76 Å, b=13.20 Å and c [fiber axis] = 5.96 Å) of the crystalline α-form P3HB phase [11]. Fiber (I) contained processing aids that give rise to an additional equatorial peak in the WAXD patterns at about 21° (indicated with a star). This peak arises from poly-ε-caprolactone (PCL) which has the (110) equatorial peak at this exact location [22]. In our previous publication, we see also the (200) PCL peak, which is located next to the (110) peak of PCL in

WAXD patterns with a larger angular range [8]. In-situ WAXD patterns of fibers (I) and (II) are shown in **Figure 2** for no applied tensile stress and for high tensile stress.

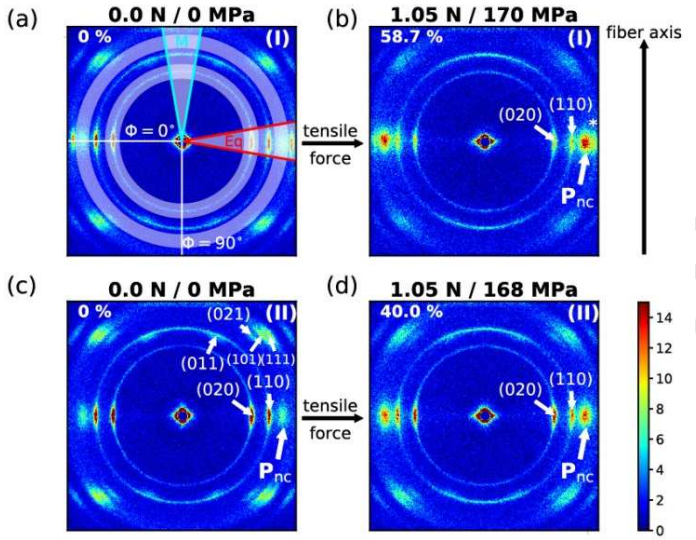


**Figure 2.** In-situ WAXD patterns (**a, b**) of fiber (I) and (**c, d**) of fiber (II), for no applied force and for a force of 1.05 N, respectively. The equatorial, Eq, and meridional, M, sectors (20° opening angle) are indicated with red and cyan colored lines, respectively. The annular regions (020) (2Θ=12.3-14.5°) and $P_{nc}$/(021) (2Θ=18.2-20.2°) are shaded in grey. Pronounced (hkl) reflections arising from the α-form P3HB phase are labeled in (**c**).

A broad equatorial reflection is clearly visible for both fibers in the region between approximately 17.8° and 20.5° in **Figure 1** as well as in Figure 2, and is labeled as $P_{nc}$. This reflection has commonly been assigned to arise from a *(para)crystalline* form of P3HB referred to as ’β-form’ [7, 9, 10, 12-16]. This β-form of P3HB has typically been considered to be generated from transformed non-crystalline regions between lamellar α-crystals, either from the tie chains between the lamellae or from completely free chains in the non-crystalline domain [7, 10, 14, 15, 23-25]. Recently, Phongtamrug and Tashiro et al.[17] have proposed that parts of the α-crystals are stressed and change to β-form crystals. Most of these recent publications discuss

the β-structure in highly drawn (10 times or more) melt-quenched P3HB films. We propose an alternative explanation for the equatorial peak in our melt-spun P3HB fibers: a highly oriented *non-crystalline mesophase*, $P_{nc}$, which is also mainly located between α-form crystals. This proposed structure is closely related to the previously proposed *(para)crystalline* 'β-form' in the sense that the newly proposed structure is also made of highly stretched molecules which are oriented along the fiber axis. However, the newly proposed model differs from the *(para)crystalline* 'β-form' model in the following points: 1. The newly proposed $P_{nc}$ mesophase is based on a non-crystalline structure where the chains do not exhibit a regular lattice ordering (e.g. hexagonal or cubic). 2. The spatial arrangements of atoms of the molecules (conformations) in the $P_{nc}$ phase depend on how much the individual chains are stretched (stretch factor) and are not represented by a well-defined planar zigzag 'β-form' conformation. In the latter conformation the atomic positions are repeated along the chain axis by a simple translation and the bond lengths, bond angles and torsion angles are well-defined [14]. In the proposed mesophase however the bond angles, torsion angles and bond lengths and thus the *x,y* positions of the atoms in the molecular chains do not repeat along the chain axis but are rather irregular. 3. The chains are not equidistant to one-another.

Similar mesophases have been proposed for other polymers in the past [26-30]. Note that we use the term 'mesophase' to describe an intermediate phase between amorphous and crystalline. The following arguments lead us to suggest this $P_{nc}$ model for our melt-spun fibers:

i) **Broadness of the equatorial reflection:** The additional equatorial reflection is broad along the equator ($\Delta 2\Theta_{Pnc} = 2°$), which implies that it is unlikely that this peak arises from a periodic crystal structure unless it would arise from poor crystals with very small sizes (< 4 nm). The broadness of the peak rather indicates a range of distances between highly

oriented molecules in the $P_{nc}$ mesophase. These distances are expected to be poorly defined and to cover a range of distances that is closely related to the dimensions of the molecules themselves. Such geometrical considerations are summarized in subsection 1.2.

ii) **Other amorphous fibers show similar equatorial reflections:** We have already observed similar equatorial reflections for various drawn fibers melt-spun from amorphous polymers [18, 31, 32].

iii) **No additional sharp off-axis WAXD reflections:** Additional reflections in the WAXD pattern should be observed if a distinct crystalline structure exists. However, no additional off-axis reflections or streaks have been observed in our study, which suggests that the chains of the mesophase have conformational disorder [33]. As mentioned before previous authors have observed a streak above the first layer line, which is however not visible in our WAXD images (**Figure 1**). Note that the angular range is large enough to cover the region above the first layer line in **Figure 1**. In an earlier study, we have also performed WAXD measurements with a larger *q*-range using Mo-$K_\alpha$ radiation. Also these WAXD images do not show any streaks or spots above layer lines of the α-form [8]. The visibility of a periodicity along the drawing axis apparently seems to largely depend on the stretch factor (draw ratio) and on how the material in question is produced. In, e.g., stretched P3HB films [12], uniaxially cold-stretched PHBV films [14] and stretched and annealed P3HB films [9, 34], weak streaks above the first layer line have been observed. However, in our melt-spun P3HB fibers [8], in melt-spun and ice water cooled P3HB [35] and P3HBV fibers [36], as well as in melt-spun P3HBV fibers [37], no such layer line streaks are visible. Phongtamrug et al.[17] are the first and to the best of our knowledge the only authors that have reported many additional distinct diffraction spots above layer lines of the α-form by subtracting a

diffraction pattern of a pure α-phase WAXD image from a mixed phase α+β WAXD image of a cold drawn P3HB film.

We propose that the outer parts of helical molecular chains from α-form crystallites transform into extended chains under tensile strain. The applied tension promotes a high orientation of the polymer chains along the fiber axis, with a range of lateral distances between the chains. Note, that helical chains can be easily extended due to the low Young's modulus, $E_c$, of α-form crystals along the chain axis which is only 5.0 GPa [11].

### *1.2. Geometrical considerations: distances between P3HB molecules*

During the transformation of α-form crystals into $P_{nc}$, the α-P3HB molecules with $2_1$ helices are deformed into stretched chains where the atoms occupy different spatial arrangements (conformations). Compared to the original $2_1$ helix, the latter stretched conformations need more space in the direction of elongation, whereas the space needed in the lateral direction is reduced. This affects the average distance between the P3HB chains. The lateral distance between two $2_1$ helical chains follows from the crystal structure of α-P3HB [11] and is subsequently denoted by *d*, which corresponds to the calculated value of the (020) reflection in α-P3HB, i.e. $d=d_{(020)}$ = 6.58 Å [11]. To estimate the effect of the elongation of P3HB molecules on the average lateral distance between the chains, either a 2-dimensional (2D) or a 3-dimensional (3D) approach can be adopted by assuming that the volume stays constant.

In a 2D approach, the area spanned by two adjacent helical molecules of distance d=6.58 Å and height $h_1=c/2$=2.98 Å [11, 12, 38] is deformed to a new area which is spanned by two nearly

planar zigzag chains of unknown distance $d_{2D}$ and estimated height $h_2$=4.60 Å [14], with the proportionality factor $F_p$=4.60/2.98=1.54. Assuming a constant area, it follows:

$$d_{2D} = \frac{d \cdot h_1}{h_2} = \frac{6.58}{1.54}\ \text{Å} = 4.27\ \text{Å} \qquad \text{(Eq. 1)}$$

with a corresponding 2Θ value of 20.8°.

In a 3D approach, we assume a constant volume. Hence,

$$V = d^2 \cdot h_1 = d_{3D}^2 \cdot h_2$$

$$d_{3D} = \frac{d}{\sqrt{F_p}} = \frac{6.58}{\sqrt{1.54}}\ \text{Å} = 5.30\ \text{Å} \qquad \text{(Eq. 2)}$$

with a corresponding 2Θ value of 16.7°. When we consider the results of the 2D and the 3D approach as extreme values, we can expect the reflections of the highly oriented non-crystalline phase $P_{nc}$ to occur in the 2Θ range between 16.7° and 20.8°. This calculated angular range matches very closely with the observed range (17.8° to 20.5°) in our experimental WAXD patterns. We conclude that the broad shape of the equatorial peak can be explained by the various distances (4.33 to 4.98 Å) between the aligned P3HB chains in the highly oriented mesophase $P_{nc}$.

### *1.3. Molecular dynamics simulations and calculation of scattered intensity*

Molecular dynamics simulations were carried out to elucidate the changes in the conformation of a P3HB chain during a uniaxial stretching parallel to the chain axis. The initial conformation of the P3HB chain was taken from the helical structures in the α-form crystal unit cell previously published by Wang et al. [11]. The non-bonded and bonded interactions were defined according to the recent implementation of the General AMBER Force Field (GAFF) used for P3HB [39]. This description of the P3HB chain in GAFF combines the standard 12-6 Lennard-Jones potential and electrostatic interactions for non-bonded interactions, with bond, angle, and

dihedral potentials for bonded interactions [40, 41]. The details are given by Glova et al. [39]. Our starting orthogonal simulation box contained a helical α-P3HB chain with 46 monomers and was deformed parallel to the chain axis until its dimension was scaled by a predefined stretch factor. This factor was set to 1.54, 1.7, and 2 in different simulations. After the deformation step, the atoms with the maximum and minimum positions along the chain axis were frozen in space and the rest of the atoms were free to equilibrate. The simulation time step was 0.5 fs with the overall run time of 1 and 1.5 ns for the deformation and equilibrium steps, respectively. The temperature was fixed during the entire simulation at 298 K. **Figure 3** shows the evolution of the chain conformation during elongation for a final stretch factor of 1.7.

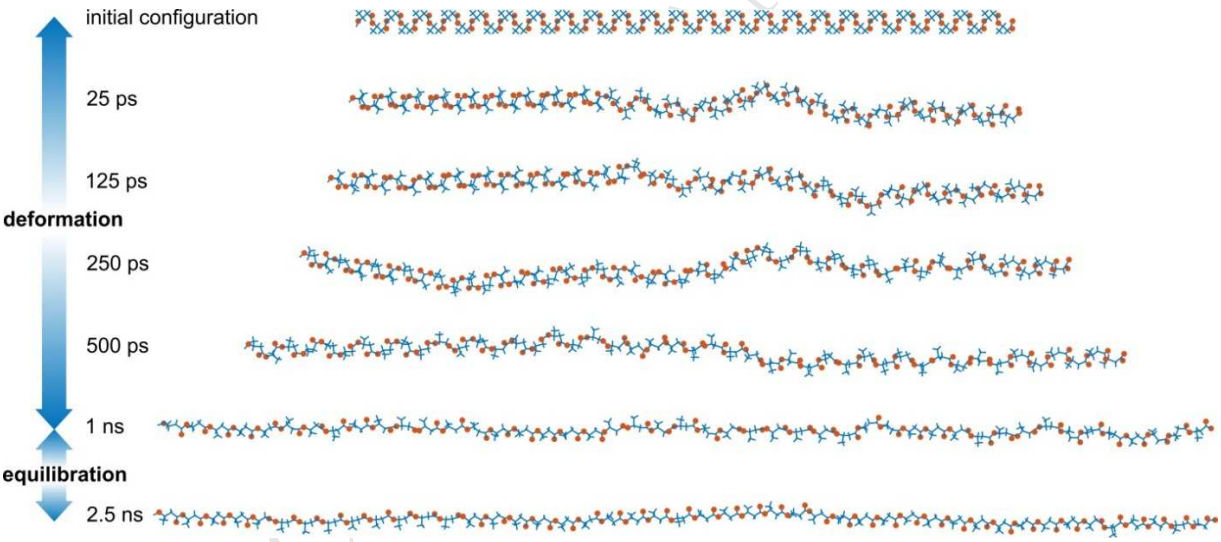


**Figure 3.** The stretching and relaxation of a P3HB chain in molecular dynamics simulations. The simulation box is stretched parallel to the chain axis by a stretch factor of 1.7 during the deformation step. The oxygen atoms are shown as red spheres along the chain.

A similar molecular dynamics simulation of the stretching behavior of a P3HB chain with 32 monomers has been previously performed by Tanaka et al. [16]. Depending on the stretch factor,

different chain conformations are obtained. The simulated torsion angles from Tanaka [16] and Orts [14] et al. are compared to our calculated torsion angles for different stretch factors in the data in brief article [18]. In the following part, we have performed scattered intensity calculations in order to show that an irregular non-crystalline structure of highly-oriented and stretched P3HB chains leads to similar scattered intensity patterns as the observed ones. Specifically, we have calculated the scattered intensity from a box of 1000x1000 stretched, oriented and identical chains. These chains are irregularly distributed on the *xy* plane. The relative positions of the atoms within one single chain were extracted from the molecular dynamics simulations for a stretch factor of 1.7 after equilibration [18]. The molecular structure factor was calculated as follows:

$$\mathrm{F_{mol}} = \sum_{\mathrm{j=1}}^{\mathrm{N_{at}}} \mathrm{f_j} \exp\left(-\mathrm{i}\left(\mathbf{q}\cdot\mathbf{R_j}\right)\right) \qquad \text{(Eq. 3)}$$

with $|\boldsymbol{q}|=4\pi\sin(\Theta)/\lambda$ the momentum transfer, $\boldsymbol{R_j}$ the spatial position of the j$^{th}$ atom, $f_j$ the atomic form factors [42] and $N_{at}$ the number of atoms in the simulated chain. The 3D scattered intensity per monomer of a box of 1000x1000 chains with $N_m$ monomers per chain is then proportional to:

$$I(\boldsymbol{s}) \propto \frac{1}{N_m N^2}\left|\sum_{p=1}^{N}\sum_{q=1}^{N} F_{mol}\ \exp\left(-i\left(\boldsymbol{q}\cdot\boldsymbol{R_{p,q}}\right)\right)\exp\left(-i\left(\boldsymbol{q}\cdot\Delta\boldsymbol{c_{p,q}}\right)\right)\right|^2 \exp\left[-\frac{\left(\mathrm{q_{xy}^2}\Delta\mathrm{X_{xy}^2}\right)}{3}\right] \text{(Eq. 4)}$$

With $\boldsymbol{q}$ the momentum transfer and $\boldsymbol{R_{p,q}}$ are the positions of the molecules along the *x*-axis (parallel to *a*) and *y*-axis (parallel to *b*), respectively. Here the distances between the chains $\Delta\boldsymbol{x_{p,q}}, \Delta\boldsymbol{y_{p,q}}$ follow a normal distribution function with a mean spacing of 4.6 Å and a standard deviation of 0.16 Å. To the best of our knowledge no higher order reflections on the equator have been reported up to now. We have therefore, introduced the Debye-Waller-factor ($DWF = \exp\left[-\frac{\left(\mathrm{q_{xy}^2}\Delta\mathrm{X_{xy}^2}\right)}{3}\right]$), which corrects the intensity for the disorder of the first kind that arises from thermal vibrations or atomic displacements [43]. A displacement of the atoms in the

*xy*-plane of $\Delta X_{xy}$ =2Å was used in the simulation and the out-of-plane displacement was set to zero. This DWF leads to a suppression of higher order reflections at larger in-plane momentum transfers $q_{xy}$. The fact that a large displacement of the atoms is needed to suppress the higher-order reflections confirms that molecular chains of different conformations are part of the $P_{nc}$ phase. The individual chains in the $P_{nc}$ phase might have different stretch factors and some may be entangled. Furthermore, we believe that the chains in the $P_{nc}$ are being stretched when a force is applied and thus their conformation changes. The factor $\Delta \boldsymbol{c}_{\boldsymbol{p,q}}$ represents the slippage of the chains along the fiber axis**.** For simplicity we have used the same molecular structure factor in the calculation of the scattered intensity for all molecules even though molecules of different conformations might better represent the effective $P_{nc}$ mesophase. Note that this proposed model is very similar to the paracrystalline model with a disorder of 2$^{nd}$ kind [44-46]. The difference is that the newly proposed model is not based on distortions of a crystal lattice with a defined unit cell but instead on a set of molecules, which are strongly disordered but highly oriented. Intensity calculations of randomly distributed chains of 20 different snapshots of the equilibrium conformations (same stretch factors) lead to similar scattering patterns as the ones shown in **Figure 4** for a set of chains with identical chain conformation.

In order to visualize the intensity scattered onto a 2D detector, the 3D intensity distribution in reciprocal space is projected onto the plane spanned by the in-plane momentum transfer $q_{xy} = \sqrt{(q_x)^2 + (q_y)^2}$ and the out-of-plane momentum transfer $q_z$. **Figure 4** shows the calculated scattered intensity of a set of stretched molecules (stretch factor 1.7) with irregular spacing and no slippage along the chain axis (**Figure 4a**) and with random slippage between -1 Å and +1 Å (**Figure 4b**). The off-axis reflection (1) is a result of the monomer repetition along the chain axis, where the positions of the oxygens along the chain axis reflect the positions of

high electron density. The vertical distance between the monomers is in average about 4.8 Å for the stretched molecule retrieved from molecular dynamics simulations.

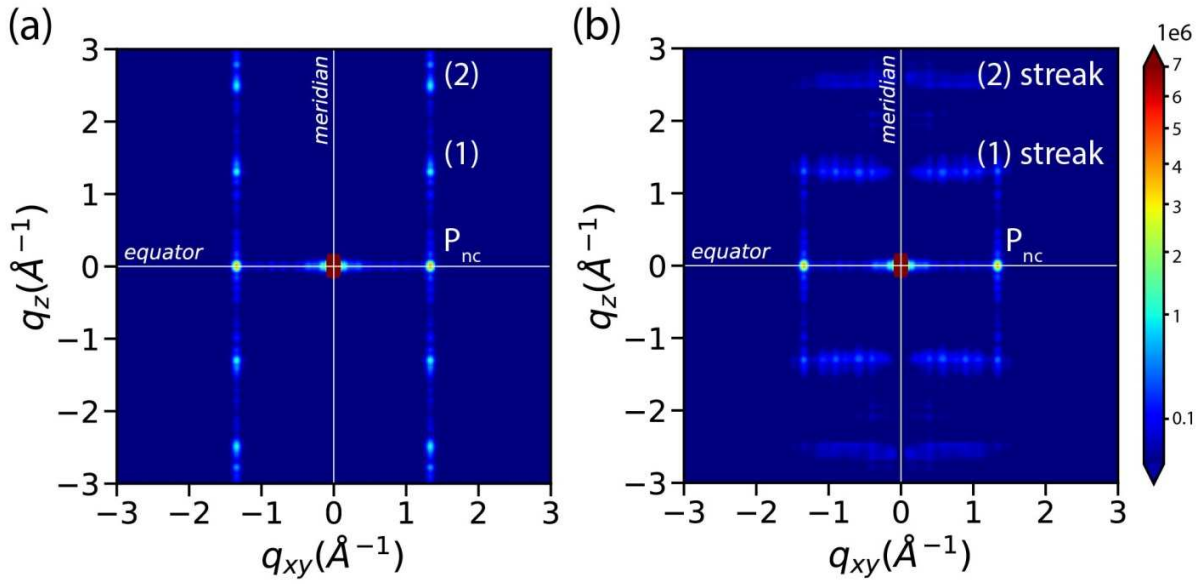


**Figure 4.** Calculated scattered intensity for (a) a set of stretched chains that are irregularly placed on the *xy* plane with no slippage along the chain axis and (b) with a random slippage in the range of -1 Å to +1 Å.

The slippage of chains along the chain axis leads to very weak streaks (one order of magnitude smaller than the $P_{nc}$ peak). Depending on the instrumental background, such streaks may or may not be observed. For large chain slippage (> 2 Å) the off-axis streaks disappear [18]. Additionally, we see for smaller stretch factors, that the out-of-plane distances between the monomers is not regular anymore and only the $P_{nc}$ peak remains. The latter would also be the case for a mixture of differently stretched molecules that are highly oriented but irregularly arranged. For large stretch factors the position of the off-axis reflection can shift depending on the vertical distances between the oxygens.

With these calculations we have shown that a non-crystalline oriented structure can generate a strong equatorial peak as well as off-axis reflections/streaks. For our fibers we did not see off-axis reflections/streaks most-likely because the molecules in the $P_{nc}$ phase of fibers with no applied tensile force were not stretched enough to get a distinct repeat unit of the oxygens along the chain axis.

### *2. Increasing intensity of equatorial $P_{nc}$ reflection with increasing tension*

In order to investigate the origin of the increase in the intensity of the $P_{nc}$ peak under tension, we have summed the WAXD patterns along the azimuth (360° in $\phi$). The corrected intensity is plotted against $2\Theta$ in **Figure 5a** for fiber (I). The dotted curves show the summed intensity of the WAXD patterns along the azimuth omitting the equatorial sectors with opening angles of 20°. The background in the (020) annulus and the (110) annulus is approximated with a linear function. Thus, the dotted curves arise from the amorphous phase and the (021) peak. The background below the $P_{nc}$ phase is almost constant since the (021) peak intensity decreases with applied tension [18] and the amorphous background increases in this region. These changes are almost cancelling out leading to an almost constant background in this angular range. Subtracting the dotted curves from the full curves leads to the integrated (020) and (110) annuli and the $P_{nc}$ peak (**Figure 5b)**. These three peaks were fit with Pearson VII functions and the calculated percentages from the peak areas are given in **Figure 5c.** The percentages of the equatorial α-form reflections, (020) and (110), were directly extracted from the 2D WAXD images by summing the intensity over the background corrected rectangular masks around the equatorial reflections and dividing the sum by the total counts between 10 and 20.4 degrees.

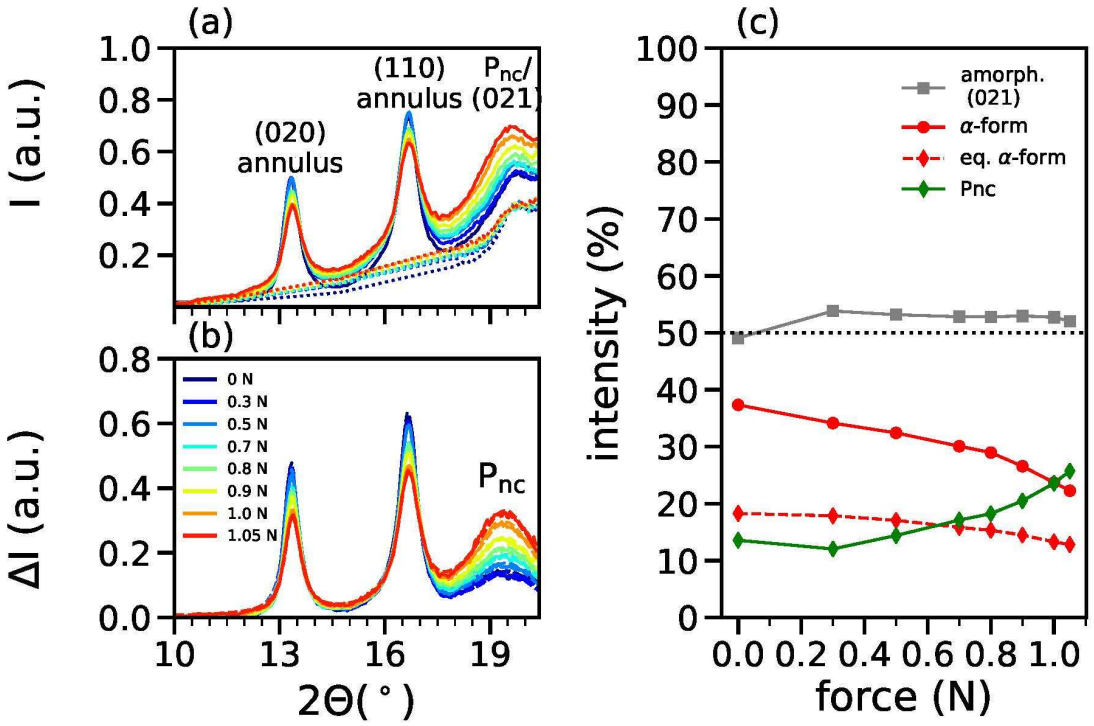


**Figure 5.** (a) Summed and normalized intensity (sum over azimuth, 360° in ϕ) for fiber (I) for increasing tension. The intensity (background) arising from the amorphous phase and the (021) peak is shown with dotted curves. (b) Background corrected intensities showing the (020), (110) annuli peaks and the $P_{nc}$ peak. Fits with Pearson VII functions: dashed lines. (c) The percentage of the amorphous phase and (021) peak intensity is shown as grey squares. The crystallinity of α-form (oriented and unoriented) is shown as red circles. The percentages of the equatorial α-form peaks are shown as red diamonds. The percentages of the $P_{nc}$ phase are shown as green diamonds.

The α-form crystallinity is decreasing from 37% (at 0 N) to 22% (at 1.05 N), whereas the sum of the $P_{nc}$ phase is increasing from 14% (at 0 N) to 26% (at 1.05 N). The amorphous phase is slightly increasing from 0 N to 0.3 N. For higher forces, however, it stays practically constant.

The α-form crystallinity is reduced to approx. 60 % of the initial value when 1.05 N is applied. Hence, about 60 % of the α-P3HB crystallites stay unaffected. The remaining 40 % of the α-form crystallites are mainly transformed into the $P_{nc}$ phase.

### *3. Coupled increase-decrease of the intensity of equatorial reflections*

In order to illustrate the effect of the applied tension on the equatorial intensity distribution, we have extracted the 2Θ profiles from the equatorial sector shown in **Figure 2a**. The resulting equatorial profiles are shown in **Figure 6a** for fiber (I) and **Figure 6b** for fiber (II), respectively. The PCL peak (110) is indicated with a star in **Figure 6a.**

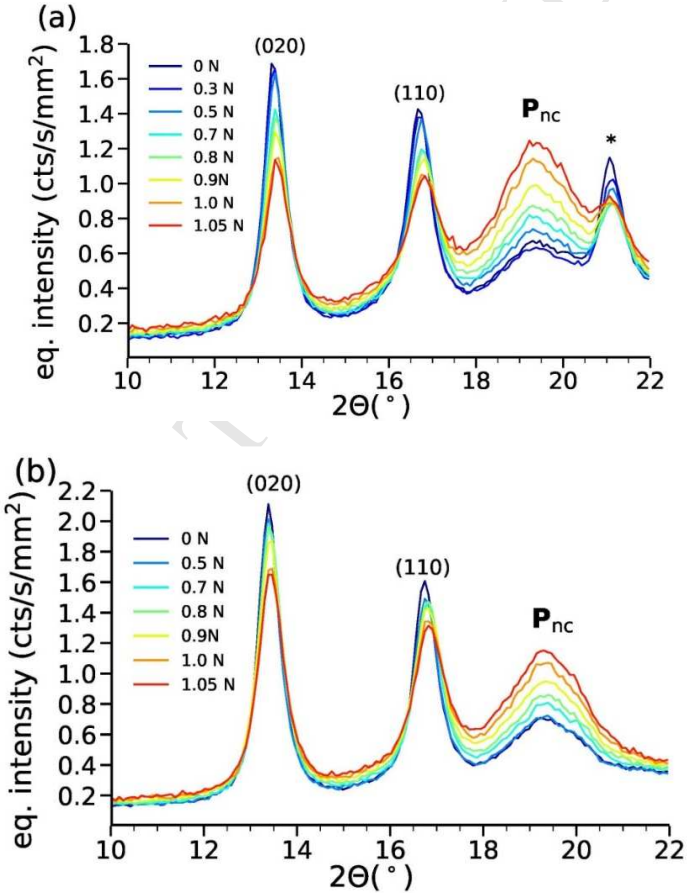


**Figure 6.** Equatorial profiles of the WAXD patterns of (a) fiber (I) and (b) fiber (II) for various applied forces. For details about the intensity corrections see the data in brief article [18].

The effect of applied tension on the WAXD pattern is the same for both fibers: an increasing tension causes a decrease in intensity for the highly oriented equatorial (020) and (110) reflections of the crystalline α-form while the broad peak labeled with $P_{nc}$ increases. The PCL processing aid in fiber (I) seems to have no particular effect on the P3HB structure since the same trends are observed for both fibers. A similar coupled increase-decrease behavior for the equatorial peaks has been previously observed for P3HB and poly(3-hydroxybutyrate-co-3-hydroxyvalerate) (PHBV) films, respectively [34, 47].

The decrease in intensity of the equatorial (020) and (110) reflections can be caused by either a loss of orientation for parts of the highly oriented crystallites or by their partial dissolution, i.e. a transformation into another crystalline modification or into a non-crystalline mesophase or into an amorphous phase.

## *4. Orientation and d-spacings of α-form crystallites*

### *4.1 Azimuthal profiles: Orientation and intensity changes*

Azimuthal profiles are shown in **Figure 7a,b** for fiber (I) and were extracted from the WAXD patterns by summing the $P_{nc}$/(021) and (020) annuli, respectively. Larger azimuthal ranges are shown in the data in brief article [18]. The orientation parameters $f_{(020)}$ of the equatorial reflection Eq(020) and $f_{Pnc}$ of the $P_{nc}$ peak, respectively, are shown in **Figure 7c.** The orientation of the $P_{nc}$ phase is clearly increasing upon drawing whereas a very small azimuthal widening of the equatorial peak, Eq(020), is observed, and thus only a small decrease in the orientation factor of these highly oriented α-crystals occurs. The equatorial peak, Eq(020), results from 'equatorially aligned α-form crystals', which have the *c*-axis aligned along the fiber axis [18]. Overall, the

alignment of the (020) planes parallel to the fiber axis is high since the orientation factor determined from Eq(020) is close to 0.9. The changes in the peak areas as a function of applied force with respect to the initial peak area, measured at zero force are plotted in **Figure 7d.** It can be seen that above an applied force of 0.5 N, the increase of the intensity in the $P_{nc}$ phase overcompensates the small intensity loss of the equatorial α-form peak.

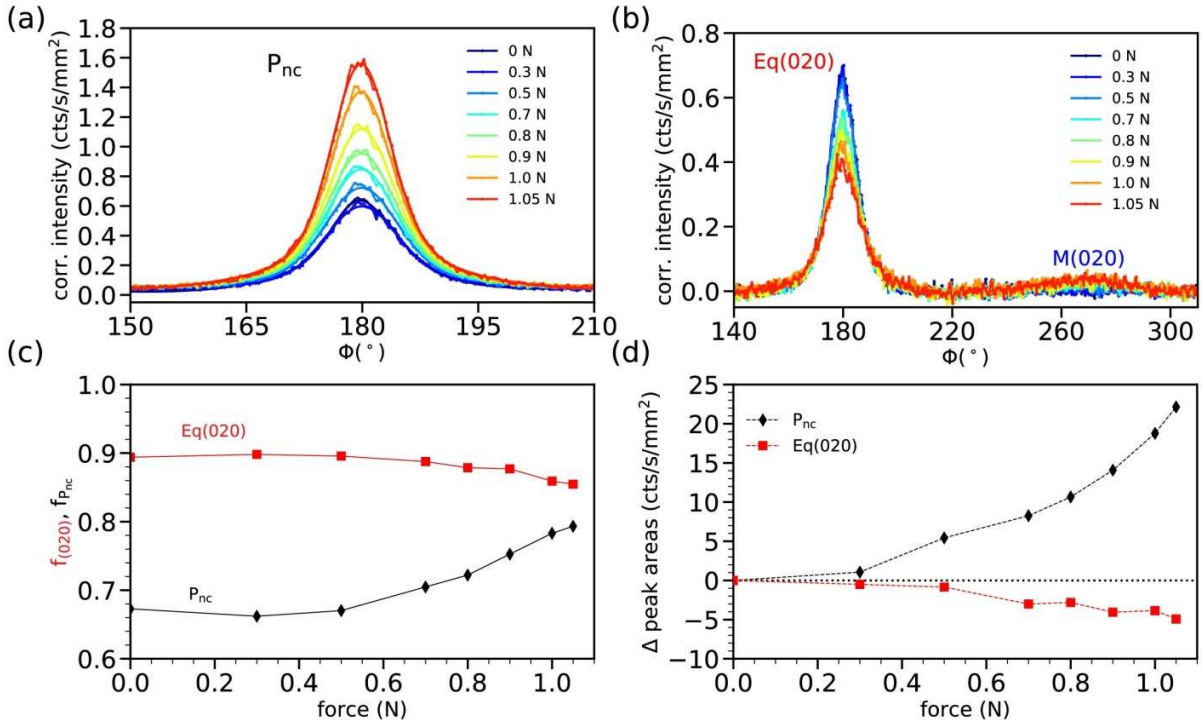


**Figure 7.** Azimuthal profiles of the $P_{nc}$/(021) annulus (a) and the (020) annulus (b) of fiber (I) for various applied forces. The ϕ angles of 180° and 270° correspond to the equatorial and the meridional direction, respectively. (c) Orientation parameter for the $P_{nc}$ phase and Eq(020) planes as a function of applied force. (d) Changes in peak intensities with respect to the initial peak intensity for zero force, Δ peak area (cts/s/mm$^2$)= area-area(0N). The changes in the $P_{nc}$ area are shown as black diamonds, and the changes in the equatorial peak area, Eq(020), as red squares.

### *4.2 Positions of equatorial and meridional α-form reflections*

Besides the decrease in intensity, the positions of the equatorial Eq(020) and Eq(110) reflections shift to higher scattering angles, whereas the reflections arising on the meridian (meridional reflections) shift to smaller scattering angles under increasing tension. The meridional reflections (e.g. **Figure 7b**, M(020)) arise from 'transversally grown' crystals whose chains are oriented perpendicular to the fiber axis [18]. In order to illustrate this effect of the applied tension on the meridional intensity distribution, we have extracted the meridional profiles. The profiles are shown in **Figure 8**. The inset shows the measured changes in *d*-spacings (equatorial and meridional) as a function of the applied tensile force. Dashed lines indicate the calculated Bragg positions for (020), (011) and (110) planes of the crystalline α-form phase. M(020) or M(011)/M(110) reflections on the meridian only appear if the crystallites are oriented with the *b*-axis being almost parallel to the fiber axis. The shifts along the meridional and equatorial direction (inset of **Figure 8**) are clearly opposite, which means that these peak shifts are a result of real changes within the crystalline network.

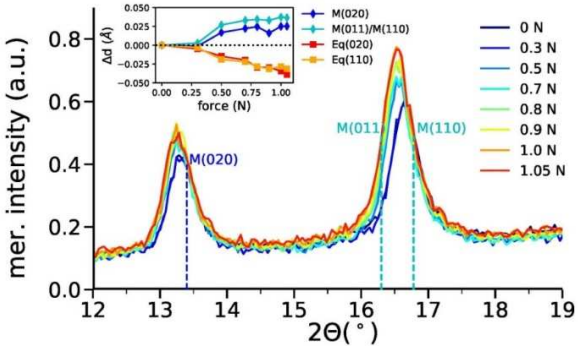


**Figure 8.** Meridional profiles of the WAXD patterns of fiber (I) for various applied forces. Dashed lines indicate the calculated Bragg positions the (020), (011) and (110) planes of the

crystalline α-form phase. Inset: extracted changes in the *d*-spacings vs. applied tensile force for meridional and equatorial peaks with respect to the *d*-spacing at zero force.

Furthermore, a force that is larger than 0.3 N is needed to compress or elongate the crystals. This critical force is very small since the helical chains can be easily extended due to the low Young's modulus of α-form crystals along the chain axis [11].

The decrease in the lattice plane distances is about 0.04±0.005 Å (data in brief [18]). Considering the compressive and tensile forces acting on the fiber, a decrease of lattice plane distances perpendicular to the fiber axis and an increase of the distances along the fiber axis are apparent.

We have verified that the changes in the meridional peak intensities, as well as shifts, are reversible to a high extent with cyclic tensile loading. This finding suggests that transversally aligned crystals are extended along the fiber axis under tensile stress, and that they snap back to the original dimension when the stress is removed.The question arises if this increase-decrease behavior of the equatorial intensities is also reversible or not.

### *5. Structure reversibility under cyclic loading*

To check for the reversibility of the intensity changes in the WAXD pattern of the P3HB fibers, fiber (I) was subjected to a cyclic change in tensile loading. Selected load-elongation curves are shown in the data in brief article [18]. The equatorial profiles extracted from the WAXD patterns that were measured at specific applied forces are shown in **Figure 9a**. The changes in the peak intensities of the α-P3HB and the $P_{nc}$ are reversible to increasing or decreasing tensile loads between 0 and 0.5 N (~80 MPa) as is shown in **Figure 9b**. After an application of 0.9 N only part of the α-P3HB peak intensities is recovered at 0.18 N, whereas the

intensity of the $P_{nc}$ is reversible to a high extent. This reversibility speaks for a reversible transformation of parts of the α-form crystals into the $P_{nc}$ phase and back.

The initial $P_{nc}$ at zero force is most-likely in a metastable frozen state. The gain in entropy upon recoiling of the stretched molecules between the lamellae would be very small due to the small restoring force acting on the stretched chains. Van der Waals forces between the chains seem to be strong enough to keep the stretched molecules in place. Additionally, we suspect that chain entanglements at the α-crystal surfaces prevent further recoiling of the chains. Upon heating without applied stress, one would however expect the molecules to recoil into helical form. In contrast if stress is applied during the heating, the stretched molecules will not recoil because they are trapped in-between the α-crystals.

The key to explain the reversibility of the transformation of the highly-oriented α-form crystallites into the $P_{nc}$ phase and back lies in the structural changes of the P3HB chains during the deformation process and their impact on the potential energy of the molecules. Tanaka et al. [16] propose a two-step mechanism for the tensile deformation process of α-form P3HB molecules which involves 1) a deformation of the helical chains to a zigzag structure with β-form conformation [14] and 2) a spring-like deformation of the zigzag chain, where the restoration force strongly increases with increasing strain. In contrast to the large restoration force in the second step, during the first step the restoration force is very small, thus when the stress is removed, the β-form molecule will largely retain its strain.

Applying this two-step deformation concept to the reversibility behavior seen in P3HB fibers under cyclic tensile loading, the following scenario can be outlined:

***Increasing load:*** While the fiber is elongated by the increasing distance of the grips, some outer portions of the highly-oriented α-form crystallites dissolve due to tensile forces

and molecular chains are elongated leading to an increasing volume of the $P_{nc}$ phase in-between lamellae. This leads to an increase in the $P_{nc}$ peak intensity and to a decrease in the total intensity for the Eq(020) and the Eq(110) reflections. At the same time, the α-form crystals are compressed in the lateral direction, leading to decreased $d_{(020)}$ spacings. In addition, P3HB chains that are already in a stretched conformation in-between lamellae will further deform. Some of the randomly oriented lamellae also partially dissolve and contribute to the $P_{nc}$ phase, while some molecules in the amorphous regions extend and may also contribute to the increase in the $P_{nc}$ intensity.

***Decreasing load:***. The fiber relaxation is driven by the restoring force of the P3HB chains that have been deformed beyond the zigzag conformation; by contracting again, these chains can markedly reduce their potential energy. The molecules can reform part of the α-P3HB crystallites when the chains have regained the $2_1$ helix conformation (lowest potential energy). These added parts to the crystallites will then give rise to the observed re-increase of intensities of the (020) and (110) peaks (**Figure 9**).

A crystalline phase is typically not showing such an elastic and reversible behavior under tensile stress and it therefore supports our hypothesis that the $P_{nc}$ is non-crystalline. The reversibility behavior actually resembles the reversible stretching of an amorphous chain, which is studied in the fundamental theory of rubber elasticity [48].

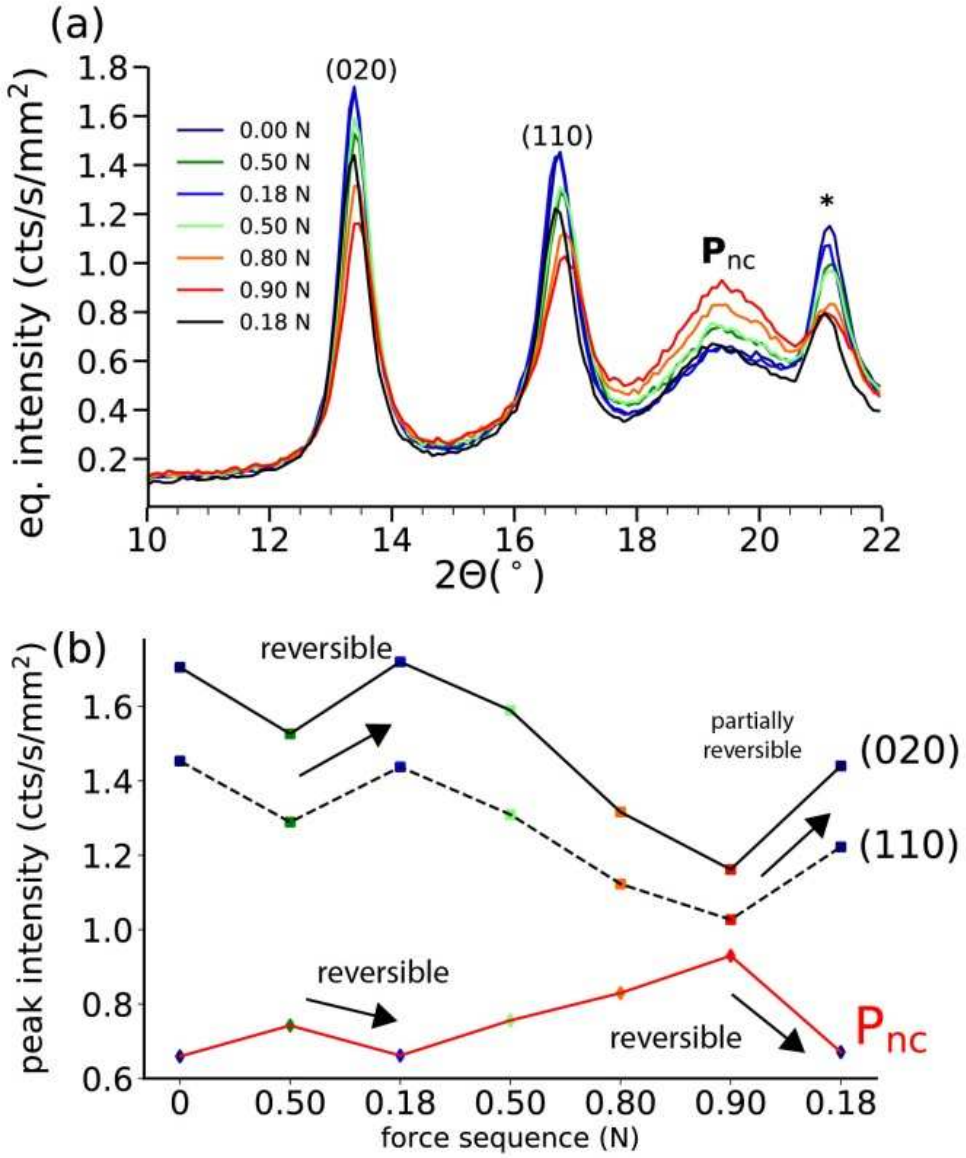


**Figure 9.** (a) Equatorial profiles of WAXD patterns of fiber (I) subjected to cyclic changes in tensile loading between 0 N and 0.9 N. The sequence of the loads follows the order indicated in the legend starting from the top. (b) Corresponding equatorial peak intensities of the α-peaks (020) and (110) as well as the $P_{nc}$ phase as a function of the force sequence. For further details regarding the cyclic loading, see data in brief article [18].

### *6. SAXS data analysis*

Selected SAXS patterns of fiber (I) for various forces during cyclic loading are shown in **Figure 10**.

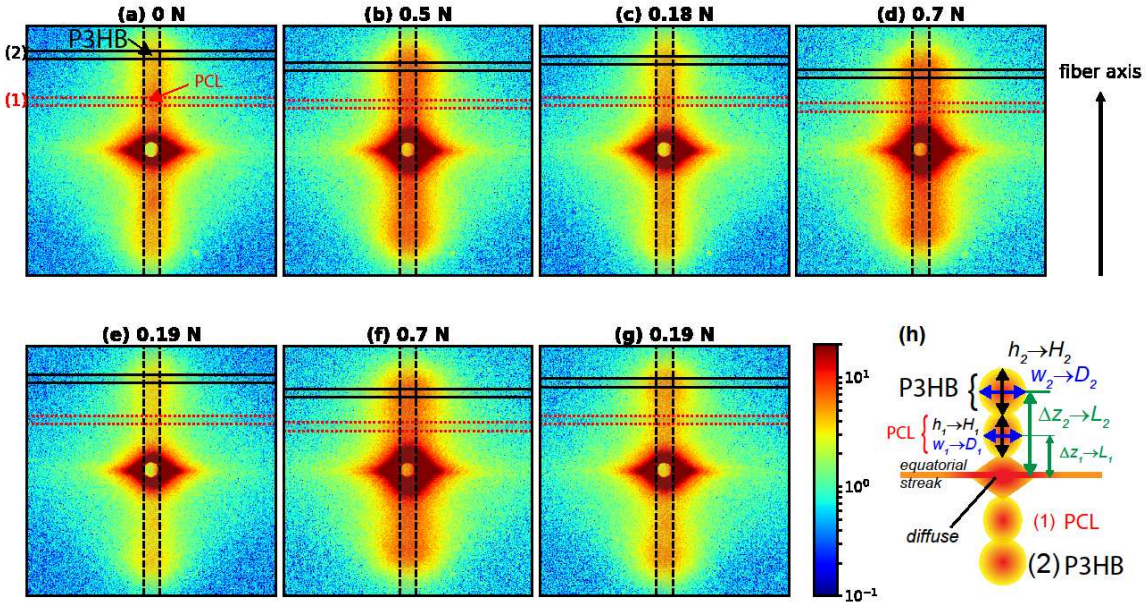


**Figure 10.** SAXS patterns measured at different applied tensions. The meridional areas are indicated with vertical dashed lines and the transversal areas for peaks (1) and (2) are indicated with red dotted and black lines. A sketch of the extraction of real space parameters from reciprocal space properties is shown in (h).

The scattering patterns show strong reflections on the meridian, which are typical for lamellae that are stacked along the fiber axis [49-51]. The equatorial streak arises from scattering objects that have a high aspect ratio and are aligned parallel to the fiber axis; such objects can either be low density regions between fibrils or lamellae or aggregates of fibrils or individual fibrils.

In order to visualize the changes to the intensity distribution along the meridian under cyclic loading, we have averaged the meridional area (black dotted vertical lines in **Figure 10**) and have plotted the resulting meridional profiles (**Figure 11**).

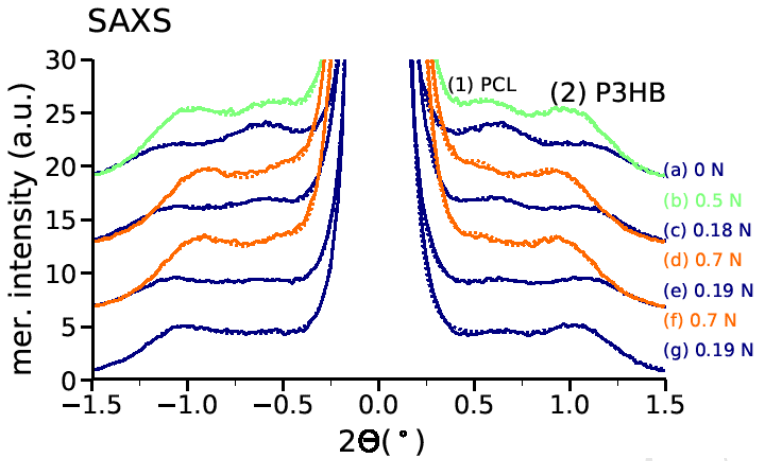


**Figure 11.** Meridional profiles as a function of diffraction angle for different applied tensions under cyclic loading. The curves are offset for better visibility.

Two symmetric reflections, (1) and (2), are clearly visible for low tensions above and below the direct beam. These meridional four-point reflections stand in contrast with the typically observed two-point reflections for lamellar structures with one single specific long-spacing [51]. We attribute this first peak to crystallites that are formed by one of the processing aids, PCL, since the peak is only present in fibers that contain PCL. Furthermore, the peak vanishes upon heating on the same time as the PCL peak indicated with a star in the WAXD patterns (heating data are not shown). The long-spacing (~15 nm) is in agreement with previously published values for PCL by other authors [52, 53]. Note that Phongtamrug and Tashiro et al.[17] have observed a significant change in their SAXS patterns of cold drawn P3HB films upon drawing including the observation of an additional peak at low *q* for higher tensions, which was attributed to a long spacing between β-crystals. They have also found a streaky SAXS peak along the equatorial line, which was attributed to a lateral period of the β-crystals. We have not seen any new peak appearing in the SAXS pattern at low *q* on the meridian for high tensions neither for

fiber I nor for fiber II and also no equatorial peak was observed in the SAXS, which speaks also against the occurrence of β-crystal bundles in our melt-spun fibers.

The meridional intensity distribution was fit with six Pearson VII functions (2 for the direct beam, and 4 symmetric peaks). The fits are shown as dotted curves, whereas the measured data is shown as full lines in **Figure 11**. Lamellar long spacings, $L_1$ and $L_2$, can be extracted from the meridional peak positions $\Delta z_1$, $\Delta z_2$ and the coherence lengths $H_1$ and $H_2$ of the lamellar stacks along the fiber direction are retrieved from the width of the lamellar reflections along the meridian. A sketch of the extraction of long-spacings, coherence lengths and diameter of lamellae from reciprocal space properties is given in **Figure 10h**. Details about the calculations and tables with the results are given in the data in brief article [18]. Lamellar diameters (sizes, *D*) were also extracted from the SAXS patterns by fitting the averaged intensity of the transversal areas to a Pearson VII function [18]. The evolution of these parameters *L*, *H* and *D* is shown as a function of the applied force sequence in **Figure 12**. Both long-spacings are increasing with increasing tension and the changes are reversible to a high extent (**Figure 12a)**. This suggests that pairs of lamellae move apart under applied tension and snap back to the original distance when the tension is decreased.

The long-spacing, coherence lengths and diameters $L_1$, $H_1$, $D_1$ are rather large for these PCL crystals, which suggests that these crystals are thin and elongated. The decrease in the crystal size during force cycling suggests that the crystals break up. The coherence lengths are only approximated values and reflect the total changes in lamellar sizes and long-spacings. The diameter of the lamellar sizes $D_2$ is slightly decreasing under applied tension with reversible changes (**Figure 12c**). The larger size $D_1$ is, however, steadily decreasing during the cycling of the applied tension (**Figure 12c,** dotted line).

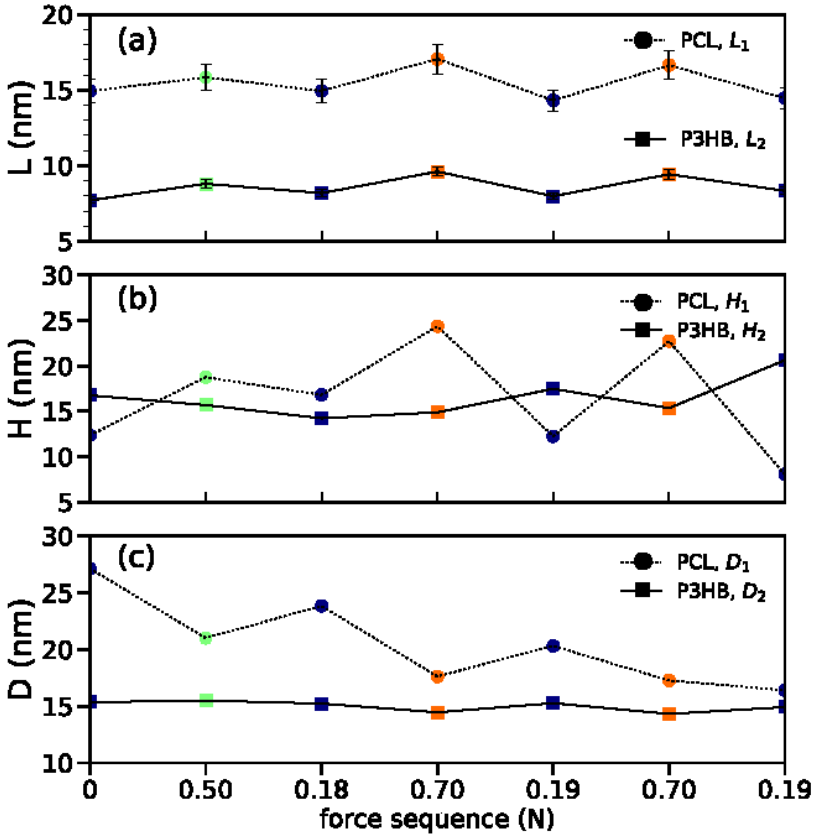


**Figure 12.** Long-spacings (a), coherence length (b) and lamellar sizes (c) as a function of consecutive applied forces. Green and orange symbols correspond to large forces and blue ones to small forces. Error bars of the long-spacings were calculated by differentiating Bragg's law and using an uncertainty of 0.3° in the 2θ angle.

Previous publications have shown two-point SAXS patterns of PHBV films with single long-spacings in the range of 7-11 nm [47] or in P3HB films with long-spacings in the range of 8 nm (low tension) to 16 nm (high tension) [34]. This matches well with the second long-spacing (7.7-9.6 nm) that we observe in our fibers and we therefore attribute the second peak to arise from P3HB α-crystals.

### *7. Structural model*

The model in **Figure 13** shows the coherently diffracting P3HB α-crystallites with the corresponding diameters, coherence lengths and long-spacings for low (0.18 N, **Figure 13a**) and medium tension (0.7 N, **Figure 13b**). The $P_{nc}$ is also shown in **Figure 13** and is located between pairs of α-crystals. This mesophase is made of stretched, irregularly arranged molecules of different conformations between α-crystals. Note that the $P_{nc}$ is not only located between α-crystals but also occurs in the amorphous part of the fiber. The extracted long-spacings of the α-crystals from the SAXS patterns are representing a mean value of a range of long-spacings that are present in the fibers. To simplify the model we are only showing the mean values for the P3HB crystallites. The exact arrangement of these pairs of crystallites (irregular or regular) in the fiber cannot be extracted from the SAXS images and remains unknown. Pairs of equatorially oriented lamellae have a long spacing of about 8 nm. Under drawing, the lamellae move apart in the fiber direction and converge laterally in reaction to a compressive force that acts perpendicular to the fiber axis (Poisson effect). As a result, the polymer chains in-between two paired lamellae extend and contribute to the $P_{nc}$ phase. Concurrently, the outmost parts of the highly-oriented lamellae dissolve and partially transform into the $P_{nc}$ phase. The height of the $P_{nc}$ phase ($L_2$-$h$) changes from 2.2 nm to 4.3 nm. The loss in the crystal height $h$ is approximately 7 Å, meaning that the chains unfold just at the outer surface of the crystal within one unit cell. The latter is just an estimation since the crystal height is estimated to be equal to the coherence length minus the long spacing. The total observed elongation is then (4.3-1.4)/2.2*100=132%. Multiplying the elongation of 132% with the percentage of the $P_{nc}$ phase, e.g. 14% at 0.18 N, leads to an expected fiber elongation of about 18% at 0.7 N. This value is remarkably close to the observed 20% fiber elongation at 0.7 N. Thus one can conclude that the observed elastic

deformation of the fiber is mainly resulting from the weak elastic elongation of the outmost helical chains of the α-phase and the further stretching of tie chains in the $P_{nc}$ phase. The reversibility of the unfolding of the outmost chains of the α-crystals is mainly seen in the WAXD intensity. Note that we do not show the crystals from the PCL phase in **Figure 13**, since we focus on the P3HB phase.

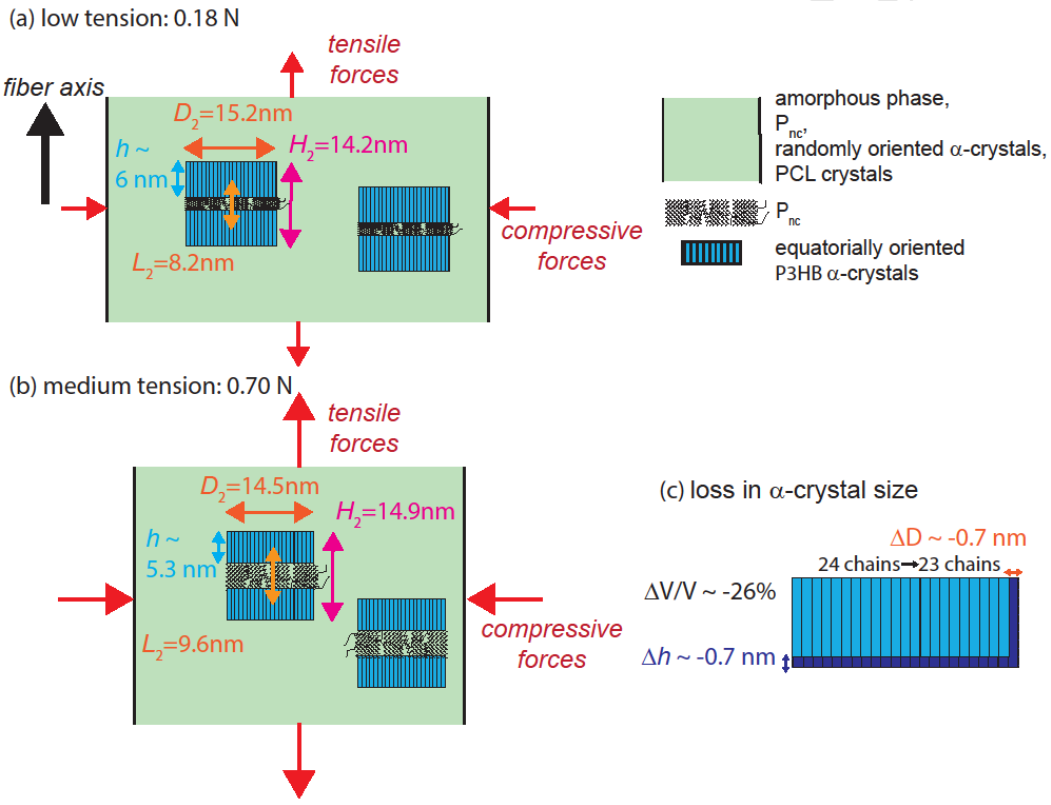


**Figure 13.** Proposed P3HB model at (a) low and (b) medium tensions. Only the highly oriented P3HB α-crystals and molecular chains in-between pairs of oriented lamellae are shown. The loss in volume of the α-crystals is schematically shown on the bottom right, (c). The dimensions of drawn lamellae and spacings are directly proportional to the values extracted from the SAXS patterns. Note that the green background area is composed of amorphous phase, $P_{nc}$ and randomly oriented α-crystals as well as processing aid crystals.

From the SAXS measurements, we can conclude that the growth of the $P_{nc}$ phase under high tension can be explained by a partial dissolution of equatorially oriented and randomly oriented α-form crystals as well as by extension and alignment of molecules in-between lamellae and in the amorphous phase.

A summary of all the observed and described effects throughout the manuscript is given in **Figure 14**.

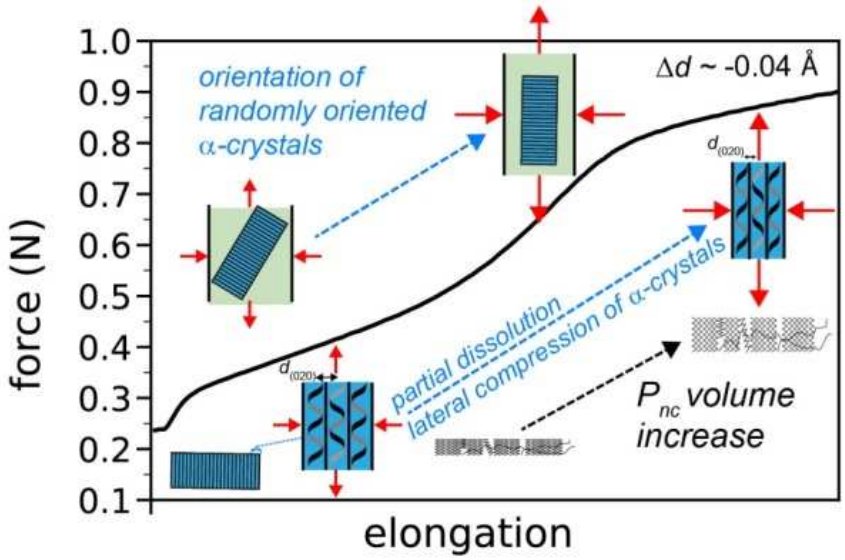


**Figure 14.** Measured force elongation curve of fiber (I) with a sketch of the various processes that happen during elongation: reorientation of α-crystals, partial dissolution and lateral compression of α-form crystals, increase of $P_{nc}$ volume.

## CONCLUSION

We propose that the additional equatorial reflection in WAXD patterns of melt-spun P3HB fibers arises from a *non-crystalline mesophase* ($P_{nc}$), which consists of highly-oriented molecules that are mainly locally trapped between α-form crystals. In this model, the stretched P3HB molecules in-between the crystals arrange in an irregular manner with varying distances**.** We suspect that this packing disorder arises due to different chain conformations and entangled chains. Under

tensile strain, α-form crystals partially dissolve and a transformation from the $2_1$ helix conformation to stretched conformations takes place, which leads to an increase of the $P_{nc}$ volume. We present major arguments from our thorough analysis of the WAXD and SAXS patterns and cyclic tensile loading experiments as well as molecular dynamics simulations and structure factor calculations that support the above proposed model. The arguments are the following: geometrical considerations about a range of molecular distances (subsection 1.2) and molecular dynamics simulations and calculations of the scattered intensity of a set of stretched chains (subsection 1.3). Experimental results: we observe an increasing intensity of the $P_{nc}$ peak under tension due to partial dissolution of α-form crystals (section 2), a coupled increase-decrease of equatorial reflections (section 3), changing *d*-spacings of laterally compressed α-form crystals under tension (subsection 4.2), highly reversible intensity increase and decrease of α-form crystals and $P_{nc}$ in WAXD patterns under cyclic loading (section 5), shrinkage and partial dissolution of α-form crystals under tension, as well as reversible long spacings between crystals under cyclic loading extracted from SAXS patterns (section 6).

We emphasize that the above described partial dissolution from α-form crystals into the $P_{nc}$ phase has an influence on the overall fiber performance and may be a versatile scheme to distribute local load in a fiber and increase tensile strength. It seems that the $P_{nc}$ alone does not provide the high tensile strength by its mere presence, but the drawing procedure itself leads to a homo-composite domain structure, which specifically provides a high tensile strength. An intimate intermixture of oriented crystalline lamellae (α-form) and non-crystalline mesomorphic regions containing highly oriented P3HB chains ($P_{nc}$) characterizes this homo-composite structure. The elastic $P_{nc}$ takes up most of the tensile forces and is uniformly distributing these forces between the rigid crystals.

AUTHOR INFORMATION

**Corresponding Author**

* E-mail address: rudolf.hufenus@empa.ch, Phone: +41 58 765 73 41

**Author Contributions**

⊥ These authors have contributed equally and are joint first authors.

DECLARATIONS OF INTEREST

Declarations of interest: none

**Funding Sources**

This research did not receive any specific grant from funding agencies in the public, commercial, or not-for-profit sectors.

ACKNOWLEDGMENT

The authors thank Manfred Heuberger and Antonia Neels (both Empa) for valuable discussions.

DATA AVAILABILITY

The raw data required to reproduce these findings are available to download from http://dx.doi.org/10.17632/h62v8nv8ck.1.

REFERENCES

[1] Dake, M., Biodegradable Polymers: Renewable Nature, Life Cycle, and Applications, in Microbial Factories: Biodiversity, Biopolymers, Bioactive Molecules: Volume 2, V.C. Kalia, Editor. 2015, Springer India: New Delhi. p. 29-56.

[2] Laycock, B., et al., The chemomechanical properties of microbial polyhydroxyalkanoates. Progress in Polymer Science, 38 (2013) 536-583. https://doi.org/10.1016/j.progpolymsci.2012.06.003.

[3] Thielen, M., Bioplastics - Basics. Applications. Markets. 2012, Mönchengladbach, Germany: Polymedia Publisher GmbH.

[4] Younes, B., Classification, characterization, and the production processes of biopolymers used in the textiles industry. Journal of the Textile Institute, 108 (2017) 674-682. https://doi.org/10.1080/00405000.2016.1180731.

[5] Leong, Y.K., et al., Current trends in polyhydroxyalkanoates (PHAs) biosynthesis: Insights from the recombinant Escherichia coli. Journal of Biotechnology, 180 (2014) 52-65. https://doi.org/10.1016/j.jbiotec.2014.03.020.

[6] Fernández-Ronco, M.P., et al., Tuning Poly(3-hydroxybutyrate) (P3HB) Properties by Tailored Segmented Biocopolymers. ACS Sustainable Chemistry & Engineering, 5 (2017) 11060-11068. https://doi.org/10.1021/acssuschemeng.7b03023.

[7] Kabe, T., et al., Physical and Structural Effects of Adding Ultrahigh-Molecular-Weight Poly (R)-3-hydroxybutyrate to Wild-Type Poly (R)-3-hydroxybutyrate. Macromolecules, 45 (2012) 1858-1865. https://doi.org/10.1021/ma202285c.

[8] Hufenus, R., et al., Molecular orientation in melt-spun poly(3-hydroxybutyrate) fibers: Effect of additives, drawing and stress-annealing. European Polymer Journal, 71 (2015) 12-26. https://doi.org/10.1016/j.eurpolymj.2015.07.039.

[9] Kabe, T., et al., Investigating thermal properties of and melting-induced structural changes in cold-drawn P(3HB) films with alpha- and beta-structures using real-time X-ray measurements and high-speed DSC. Polymer, 93 (2016) 181-188. https://doi.org/10.1016/j.polymer.2016.04.028.

[10] Pan, P. and Y. Inoue, Polymorphism and isomorphism in biodegradable polyesters. Progress in Polymer Science, 34 (2009) 605-640. https://doi.org/10.1016/j.progpolymsci.2009.01.003.

[11] Wang, H. and K. Tashiro, Reinvestigation of Crystal Structure and Intermolecular Interactions of Biodegradable Poly(3-Hydroxybutyrate) α-Form and the Prediction of Its Mechanical Property. Macromolecules, 49 (2016) 581-594. https://doi.org/10.1021/acs.macromol.5b02310.

[12] Yokouchi, M., et al., Structural studies of polyesters .5. Molecular and crystal structures of optically active and racemic poly(beta-hydroxybutyrate). Polymer, 14 (1973) 267-272. https://doi.org/10.1016/0032-3861(73)90087-6.

[13] Schmack, G., et al., Biodegradable fibers of poly(3-hydroxybutyrate) produced by high-speed melt spinning and spin drawing. Journal of Polymer Science Part B-Polymer Physics, 38 (2000) 2841-2850. https://doi.org/.

[14] Orts, W.J., et al., Observation of Strain-Induced β Form in Poly(β-hydroxyalkanoates). Macromolecules, 23 (1990) 5368-5370. https://doi.org/10.1021/ma00228a014.

[15] Yamane, H., et al., Mechanical properties and higher order structure of bacterial homo poly(3-hydroxybutyrate) melt spun fibers. Polymer, 42 (2001) 3241-3248. https://doi.org/10.1016/s0032-3861(00)00598-x.

[16] Tanaka, F., Y. Doi, and T. Iwata, The deformation of the chain molecules and crystallites in poly( R -3-hydroxybutyrate) and poly(4-hydroxybutyrate) under tensile stress. Polymer Degradation and Stability, 85 (2004) 893-901. https://doi.org/10.1016/j.polymdegradstab.2004.04.006.

[17] Phongtamrug, S. and K. Tashiro, X-ray Crystal Structure Analysis of Poly(3-hydroxybutyrate) β-Form and the Proposition of a Mechanism of the Stress-Induced α-to-β Phase Transition. Macromolecules, 52 (2019) 2995-3009. https://doi.org/10.1021/acs.macromol.9b00225.

[18] Perret, E., et al., X-ray data from a cyclic tensile study of melt-spun poly(3-hydroxybutyrate) P3HB fibers: A reversible mesophase. Data in Brief (under review), (2019) https://doi.org/.

[19] Klug, H.P. and L.E. Alexander, X-Ray Diffraction Procedures. 2nd. ed. 1974, New York: John Wiley & Sons, Inc.

[20] Hall, M.M., et al., The Approximation of Symmetric X-Ray Peaks by Pearson Type VII Distributions. Journal of Applied Crystallography, 10 (1977) 66-68. https://doi.org/10.1107/s0021889877012849.

[21] Hermans, J.J., et al., Quantitative Evaluation of Orientation in Cellulose Fibres from the X-Ray Fibre Diagram. Recueil Des Travaux Chimiques Des Pays-Bas-Journal of the Royal Netherlands Chemical Society, 65 (1946) 427-447. https://doi.org/10.1002/recl.19460650605.

[22] Bittiger, H., R.H. Marchessault, and W.D. Niegisch, Crystal structure of poly-ε-caprolactone. Acta Crystallographica Section B, 26 (1970) 1923-1927. https://doi.org/doi:10.1107/S0567740870005198.

[23] Furuhashi, Y., et al., Higher order structures and mechanical properties of bacterial homo poly(3-hydroxybutyrate) fibers prepared by cold-drawing and annealing processes. Polymer, 45 (2004) 5703-5712. https://doi.org/10.1016/j.polymer.2004.05.069.

[24] Aoyagi, Y., Y. Doi, and T. Iwata, Mechanical properties and highly ordered structure of ultra-high-molecular-weight poly (R)-3-hydroxybutyrate films: Effects of annealing and two-step drawing. Polymer Degradation and Stability, 79 (2003) 209-216. https://doi.org/10.1016/s0141-3910(02)00273-2.

[25] Iwata, T., et al., Mechanical properties of uniaxially cold-drawn films of poly( R -3-hydroxybutyrate). Polymer Degradation and Stability, 79 (2003) 217-224. https://doi.org/10.1016/s0141-3910(02)00274-4.

[26] Luo, L., et al., Pre-drawing induced evolution of phase, microstructure and property in para-aramid fibres containing benzimidazole moiety. RSC Advances, 6 (2016) 62695-62704. https://doi.org/10.1039/C6RA10184D.

[27] Ran, S., et al., Structural changes during deformation of Kevlar fibers via on-line synchrotron SAXS/WAXD techniques. Polymer, 42 (2001) 1601-1612. https://doi.org/.

[28] Ran, S.F., et al., Structural and morphological studies of isotactic polypropylene fibers during heat/draw deformation by in-situ synchrotron SAXS/WAXD. Macromolecules, 34 (2001) 2569-2578. https://doi.org/.

[29] Ran, S., et al., Structural and Morphological Studies of Isotactic Polypropylene Fibers during Heat/Draw Deformation by in-Situ Synchrotron SAXS/WAXD. Macromolecules, 34 (2001) 2569-2578. https://doi.org/10.1021/ma0016477.

[30] Ran, S.F., et al., Mesophase as the precursor for strain-induced crystallization in amorphous poly(ethylene terephthalate) film. Macromolecules, 35 (2002) 10102-10107. https://doi.org/10.1021/ma021252i.

[31] Reifler, F.A., et al., Polymer optical fibers for textile applications - Bicomponent melt spinning from cyclic olefin polymer and structural characteristics revealed by wide angle X-ray diffraction. Polymer, 55 (2014) 5695-5707. https://doi.org/10.1016/j.polymer.2014.08.071.

[32] Leal, A.A., et al., Mechanical response of melt-spun amorphous filaments. Science and Technology of Advanced Materials, 15 (2014) 11. https://doi.org/10.1088/1468-6996/15/3/035016.

[33] Auriemma, F., et al., Mesomorphic Form (β) of Nylon 6. Macromolecules, 30 (1997) 7554-7559. https://doi.org/10.1021/ma970828e.

[34] Iwata, T., et al., Time-resolved X-ray diffraction study on poly (R)-3-hydroxybutyrate films during two-step-drawing: Generation mechanism of planar zigzag structure. Biomacromolecules, 6 (2005) 1803-1809. https://doi.org/10.1021/bm050152s.

[35] Iwata, T., et al., Microbeam X-ray diffraction and enzymatic degradation of poly[(R)-3-hydroxybutyrate] fibers with two kinds of molecular conformations. Macromolecules, 39 (2006) 5789-5795. https://doi.org/10.1021/ma060908v.

[36] Tanaka, T., et al., Formation of highly ordered structure in poly[(R)-3-hydroxybutyrate-co-(R)-3-hydroxyvalerate] high-strength fibers. Macromolecules, 39 (2006) 2940-2946. https://doi.org/10.1021/ma0527505.

[37] Antipov, E.M., et al., Strain-induced mesophase and hard-elastic behaviour of biodegradable polyhydroxyalkanoates fibers. Polymer, 47 (2006) 5678-5690. https://doi.org/10.1016/j.polymer.2005.04.111.

[38] Cornibert, J. and R.H. Marchessault, Physical properties of poly-β-hydroxybutyrate. IV. Conformational analysis and crystalline structure. Journal of Molecular Biology, 71 (1972) 735-756. https://doi.org/.

[39] Glova, A.D., et al., Scale-Dependent Miscibility of Polylactide and Polyhydroxybutyrate: Molecular Dynamics Simulations. Macromolecules, 51 (2018) 552-563. https://doi.org/10.1021/acs.macromol.7b01640.

[40] Gooneie, A., J. Gonzalez-Gutierrez, and C. Holzer, Atomistic Modelling of Confined Polypropylene Chains between Ferric Oxide Substrates at Melt Temperature. Polymers, 8 (2016) https://doi.org/10.3390/polym8100361.

[41] Gooneie, A., S. Schuschnigg, and C. Holzer, A Review of Multiscale Computational Methods in Polymeric Materials. Polymers, 9 (2017) https://doi.org/10.3390/polym9010016.

[42] Brown, P.J., et al., Intensity of diffracted intensities, in International Tables for Crystallography Volume C: Mathematical, physical and chemical tables, E. Prince, Editor. 2004, Springer Netherlands: Dordrecht. p. 554-595.

[43] Guinier, A., X-Ray Diffraction: In Crystals, Imperfect Crystals, and Amorphous Bodies. 2013: Dover Publications.

[44] Hosemann, R., Crystallinity in High Polymers, especially Fibres. Polymer, 3 (1962) 349-392. https://doi.org/10.1016/0032-3861(62)90093-9.

[45] Hosemann, R. and A.M. Hindeleh, Structure of crystalline and paracrystalline condensed matter. Journal of Macromolecular Science-Physics, B34 (1995) 327-356. https://doi.org/10.1080/00222349508219497.

[46] Kasai, N. and M. Kakudo, X-Ray Diffraction by Macromolecules. 2005, Tokyo Berlin Heidelberg: Kodansha Ltd and Springer Verlag.

[47] Yang, J., et al., New insights into the beta-form crystal toughening mechanism in pre-oriented PHBV films. European Polymer Journal, 91 (2017) 81-91. https://doi.org/10.1016/j.eurpolymj.2017.03.017.

[48] Sperling, L.H., Introduction to Polymer Science, in Introduction to Physical Polymer Science. 2006, Wiley.

[49] Murthy, N.S., Small-Angle Scattering, in Structure Formation in Polymeric Fibers, D.R. Salem, Editor. 2001, Carl Hanser Verlag: Munich. p. 475-492.

[50] Murthy, N.S., et al., Analysis of small-angle X-ray scattering from fibers: Structural changes in nylon 6 upon drawing and annealing. Journal of Polymer Science Part B-Polymer Physics, 34 (1996) 821-835. https://doi.org/.

[51] Murthy, N.S. and D.T. Grubb, Deformation in lamellar and crystalline structures: in situ simultaneous small-angle X-ray scattering and wide-angle X-ray diffraction measurements on polyethylene terephthalate fibers. Journal of Polymer Science Part B-Polymer Physics, 41 (2003) 1538-1553. https://doi.org/.

[52] Oudhuis, A.A.C.M., et al., A comparison between the morphology of semicrystalline polymer blends of poly(ε-caprolactone)/poly(vinyl methyl ether) and poly(ε-caprolactone)/(styrene-acrylonitrile). Polymer, 35 (1994) 3936-3942. https://doi.org/https://doi.org/10.1016/0032-3861(94)90278-X.

[53] Kamal, T., T.J. Shin, and S.-Y. Park, Uniaxial Tensile Deformation of Poly(ε-caprolactone) Studied with SAXS and WAXS Techniques Using Synchrotron Radiation. Macromolecules, 45 (2012) 8752-8759. https://doi.org/10.1021/ma301714f.

[54] Špitalský, Z. and T. Bleha, Elastic Properties of Poly(hydroxybutyrate) Molecules. 4 (2004) 601-609. https://doi.org/10.1002/mabi.200300118.

**Highlights**

- Reversibility behavior of structural transformations in P3HB under cyclic loading.
- Detailed SAXS, WAXD analysis of P3HB fibers under cyclic loading.
- New structural model for phases in P3HB based on molecular dynamics simulations.